ELSEVIER

Contents lists available at ScienceDirect

International Journal of Applied Earth Observation and Geoinformation

journal homepage: www.elsevier.com/locate/jag





Sentinel-1 InSAR-derived land subsidence assessment along the Texas Gulf Coast

Xiaojun Qiao ^{a,b}, Tianxing Chu ^{a,b,*}, Philippe Tissot ^{b,c}, Seneca Holland ^b

- ^a Department of Computer Science, Texas A&M University-Corpus Christi, 6300 Ocean Drive, Corpus Christi, TX 78412, USA
- b Conrad Blucher Institute for Surveying and Science, Texas A&M University-Corpus Christi, 6300 Ocean Drive, Corpus Christi, TX 78412, USA
- ^c Department of Physical and Environmental Sciences, Texas A&M University-Corpus Christi, 6300 Ocean Drive, Corpus Christi, TX 78412, USA

ARTICLE INFO

Keywords: Land deformation Coastal subsidence InSAR Anthropogenic and natural impacts Sea-level rise Texas Gulf Coast

ABSTRACT

Mapping large-scale coastal subsidence is significant in providing valuable support to decision-making stakeholders to recognize impacts of potential natural disasters. However, this task presents significant challenges due to its highly complex nature of the spatial-temporal variability. Recent advances in the observation capability of synthetic aperture radar (SAR) missions and the processing algorithms of interferometric SAR (InSAR) techniques have made it possible to efficiently map large-scale subsidence from space. This study utilized the persistent scatterer (PS) InSAR method to process four swathes of Sentinel-1 SAR images captured between 2016 and 2022 to map large-scale subsidence along the Texas coastline. The subsidence map, encompassing over 1.7 million PS points, was calibrated/validated with observations of 115 continuously operating global navigation satellite system (cGNSS) stations. Nineteen subsiding hotspots were identified and potential subsidence drivers were analyzed, including hydrocarbon extraction (HE), groundwater withdrawal (GW), and salt domes. The results suggest that HE activities were the primary driver of observed subsidence in the Coastal Bend and South Texas, as well as in the Southeast Texas regions. In the Houston-Galveston Area, subsidence appears to be influenced by a combination of GW, HE, and salt dome movements. Within 50 km of the Texas shorelines, subsidence rates were approximately -1.0 mm/yr within the coastal vicinity, while inland areas experience a gradually increasing trend. Specific coastal areas, such as Corpus Christi, Freeport, Seabrook, San Leon, and others, may face elevated flooding risks during high tide and storm events with the sea-level rise trend up to 24.0 mm/yr in relation to coastal subsiding land.

1. Introduction

Natural geohazards such as earthquakes and landslides can cause significant instantaneous ground motion, resulting in various types of adverse consequences like infrastructure damage, human casualties, and economic losses to name a few. However, it is important to recognize that anthropogenic activities can also contribute to land motion. albeit in a more gradual manner. Activities like groundwater withdrawal (GW) and hydrocarbon extraction (HE), for example, can trigger subsurface rock movement, leading to land subsidence at the surface. Studies have reported that approximately 77% of land subsidence cases worldwide were a direct result of human activities (Bagheri-Gavkosh et al., 2021). Moreover, human-induced land subsidence exhibits a frequent occurrence across space and maintains consistency over time, potentially resulting in a significant accumulation in both spatial and temporal dimensions. Consequently, land subsidence has gained growing attention in academia over recent decades and has emerged as a pressing global concern (Bagheri-Gavkosh et al., 2021).

Coastal areas are particularly vulnerable to the impacts made by land subsidence due to the intricate elevation dynamics between the land and sea. On one hand, land subsidence signifies a decline in land elevation along the coast (Dinar et al., 2021), often referred to as the vertical land motion (VLM). On the other hand, global sea levels have been steadily rising since the 1870s based on the continuous measurements from a network of globally distributed tide gauges (TGs) (Church and White, 2011, 2006), and the rises in sea levels, without regard to land movement, are defined as the absolute sea-level rise (ASLR). Consequently, both human and natural systems in coastal areas are increasingly susceptible to escalated risks of flooding during high tide events and storm surges. This risk arises from the combined effects of global sea-level rise in relation to the sinking local land, a phenomenon known as the relative sea-level rise (RSLR) (Shirzaei et al., 2021). And the relationship of $v_{RSLR} = v_{ASLR} - v_{VLM}$ holds with the velocity, v, being positive in the upward vertical direction. Past findings revealed

^{*} Corresponding author at: Department of Computer Science, Texas A&M University-Corpus Christi, 6300 Ocean Drive, Corpus Christi, TX 78412, USA. E-mail address: tianxing.chu@tamucc.edu (T. Chu).

that land subsidence has been recognized as a prominent contributing factor of the RSLR in many coastal cities worldwide (Tay et al., 2022). Thus, it is imperative to monitor both the VLM and the RSLR in subsiding coastal regions, such as the Texas Gulf Coast (Tay et al., 2022).

Several instruments and techniques have been employed to observe coastal subsidence, including spirit leveling, extensometers, global navigation satellite systems (GNSS), and TG stations (Shirzaei et al., 2021; Qiao et al., 2022). The most accurate methods for measuring land subsidence involve utilizing spirit leveling at the surface and employing extensometers in the subsurface (Galloway and Burbey, 2011). Highfrequency positional information collected at continuous GNSS (cGNSS) stations, e.g., with an interval of 30 s, enables the accurate measurements of daily ellipsoid height with millimeter-level accuracy. TG stations also play a crucial and long-lasting role in reflecting subsiding processes at coasts by recording sea levels relative to attached land benchmarks (Qiao et al., 2023). However, these methods are limited to capturing elevation displacements at selected locations, which restricts their ability to unveil the highly varying nature of land subsidence. For instance, these techniques are inadequate for revealing the localized bowl-shaped subsidence patterns associated with oil and gas extraction (Buckley et al., 2003).

The interferometric synthetic aperture radar (InSAR) is a space-borne geodetic technique used to measure land deformation by differencing phase images observed at two distinct time points above the same ground under the exposure to microwave radiation. For the purpose of land deformation estimate, the interferogram undergoes a process called differential InSAR (DInSAR), wherein the phase components associated with slant range displacement and terrain height are typically subtracted using accurate orbit and digital elevation model(DEM) data (Ferretti et al., 2007). It is worth noting that the term InSAR is commonly used for land deformation monitoring and analysis despite DInSAR being the primary technique. However, isolating the phase components of deformation from a single differential interferogram remains challenging due to the influences of phase decorrelation and atmospheric effects (Ferretti, 2014).

A popular solution proposed to distinguish deformation phase components involves leveraging the atmospheric distinction characterized by both low spatial and high temporal variability through a stack of multi-temporal interferograms, using phase correlated man-made structures known as persistent scatterers (PSs) (Ferretti et al., 2001; Ferretti, 2014). The PS InSAR (PSI) technique can yield reliable land deformation results, achieving an overall velocity precision up to 1.0 mm/year. However, the practical accuracy of the technique depends on various factors such as the number of images used, the dispersion of temporal and geometrical baseline values, the density of PS, and so forth (Ferretti, 2014).

The twin Sentinel-1 satellites, launched in 2014 and 2016, respectively, have proven to be invaluable for capturing SAR images with exceptional spatiotemporal coverage. Each satellite provides a revisit period of 12 days, and they boast an impressive swath width of up to 250 km. The meticulous control of Sentinel-1 orbits has significantly minimized the dispersion of geometrical baselines, thus reducing associated decorrelation. Additionally, the use of PSI is efficient (Ferretti et al., 2001) in processing the vast amount of SAR images obtained from Sentinel-1. These characteristics make it feasible to map large-scale land deformation using the PS points of Sentinel-1 InSAR.

This research employed the PSI technique to analyze Sentinel-1 SAR images and derive land deformation information across the Gulf Coast of Texas. Relative to the previous studies, this work contributed to the literature in three perspectives. Specifically, this study (1) mapped large-scale land deformation across the areas near the Texas coastlines, utilizing available Sentinel-1 images from late 2016 until approximately mid 2022, rather than performing assessment in specific areas such as the vicinity of Houston and the Texas Coastal Bend area (Khan

et al., 2022; Liu et al., 2022; Haley et al., 2022); (2) sought to provide valuable insights into how some natural/anthropogenic activities potentially impacted land deformation at multiple subsidence hotspots along the Texas Coast and investigated correlations between them; and (3) kept a closer eye on examining subsidence near the Texas shorelines, aiming to investigate the extent to which it contributed to the RSLR and flooding risks.

2. Study area and data

2.1. Study area

The study area encompasses regions near the Texas coastlines, along the northern Gulf of Mexico (GOM) (Fig. 1). During the Tertiary and Quaternary geological periods, the coastal plains experienced cyclic sediment deposition due to shallow-marine processes and fluvialdeltaic environments, resulting in progressively thickening sediment layers towards the GOM (Chowdhury and Turco, 2006). The hydrostratigraphic divisions widely recognized for the aquifer system along the Texas Gulf Coast are as follows: the Catahoula Confining system, Jasper aquifer, Burkeville confining system, Evangeline aquifer, and Chicot aquifer (Baker, 1979). Some progradation wedges have been identified to contain deep sandstone reservoirs that are conducive to the accumulation of hydrocarbons, e.g., the Frio and Vicksburg Formations (Loucks, 1986). Throughout both the Frio and Vicksburg periods, researchers have identified three major structural provinces in the region, including the Houston embayment in eastern Texas, the Rio Grande embayment in southern Texas, and the San Marcos platform located in the central region (Galloway et al., 1982; Gregory, 1966). Curved faults running parallel to the Texas Coast have undergone syn-deposition with sediment burial processes (Chowdhury and Turco, 2006). These fault zones exert influence on both aquifer systems and the hydrocarbon accumulation by controlling the distribution and orientation of sand depocenters (Solís I, 1981; Hyne, 1984). Salt domes, exerting influence on both hydrocarbon exploration and the dynamics of local aquifers, have been reported to occur in a higher concentration in the upper Texas Coast as compared to the lower region (Chowdhury and Turco, 2006).

The Texas Gulf Coast region has acquired attention for its susceptibility to land subsidence, predominantly resulting from human and natural activities such as GW, HE, sediment compaction, and tectonic motion (Pratt and Johnson, 1926; Galloway et al., 1999; Qu et al., 2015, 2023; Haley et al., 2022). In addition, frequently observed subsidence in the Texas coastal region may also stem from salt dome formation (Qu et al., 2015). The diapir geological structure, which often contains evaporitic salt deposits (salt domes), can rise through the sediment strata (Rajput and Thakur, 2016). Salt domes can create stratigraphic traps and are often found in spatial proximity to oil and/or gas wells (Hyne, 1984). Both natural processes and human activities can cause subsidence over salt domes, primarily due to the dissolution and removal of salt (Rajput and Thakur, 2016).

2.2. SAR images

Four interferometric wide (IW) swathes of SAR data acquired between 2016 and 2022 were used in this study, corresponding to varying path and frame combinations, identified by their "path_frame" format: 136_93, 34_90, 107_88, and 107_83 (ASF, 2022). These SAR images in the ascending tracks collectively provided nearly full coverage of the Texas coastlines in terms of the spatial extent. A total of 559 SAR image were obtained and data in the VV polarization were utilized for InSAR analysis. Within each IW swath, three sub-swathes arranged in order of distance from the antenna are denoted in this study as sub-swath 1, 2, and 3, respectively. It should be noted that only sub-swathes covering the Texas Gulf Coast region were used. More details about SAR images can be found in Table 1, as well as in Table S1

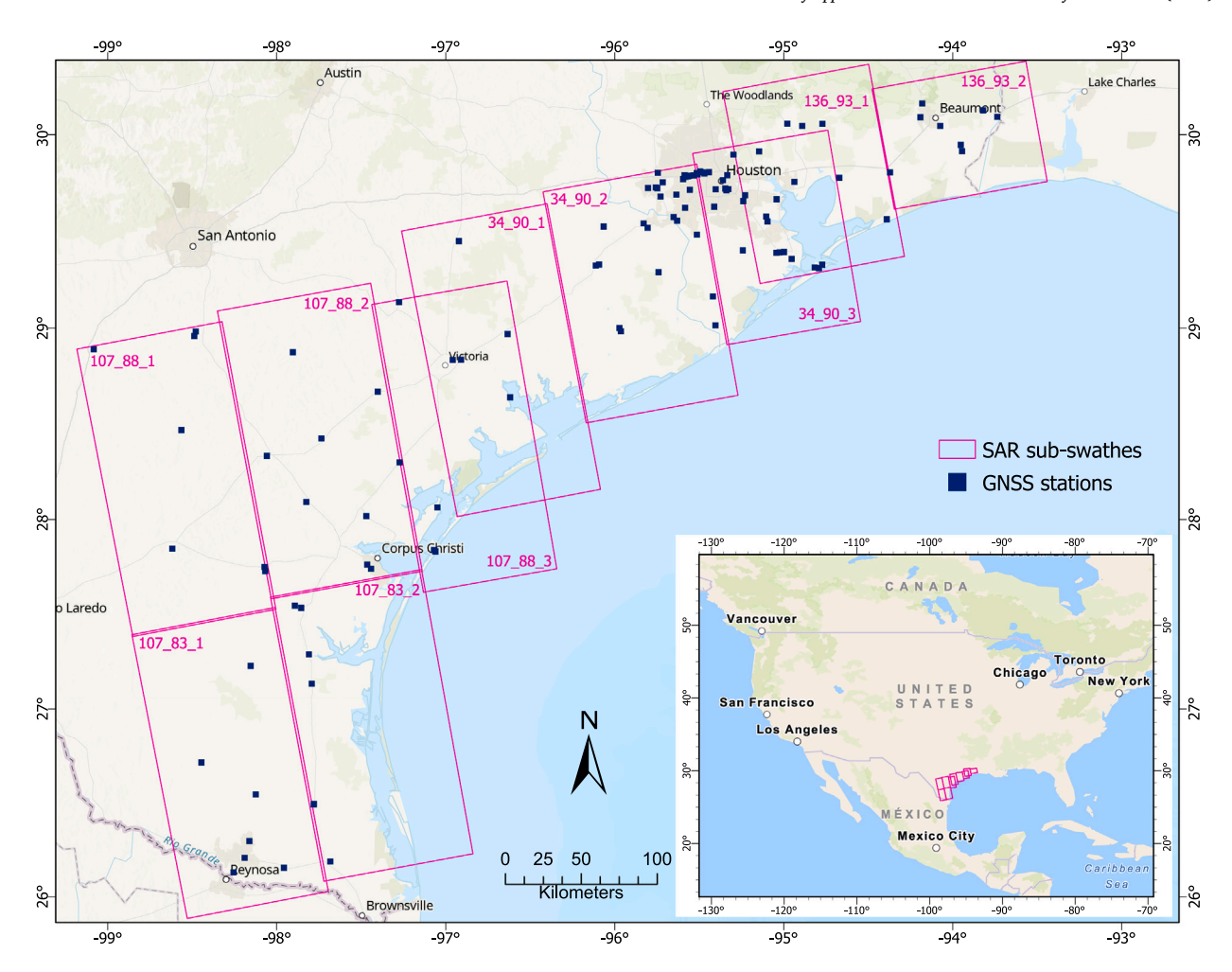


Fig. 1. Map of the focused area (i.e., coastal regions of Texas along the northern Gulf of Mexico) of SAR sub-swath images and cGNSS stations. Sub-swath name is marked at corner of the corresponding polygon in a format of "path_frame_sub-swath".

Table 1
Overview of SAR image data collections.

	136_93	34_90	107_88	107_83
Number of images	130	147	144	138
Start date	Oct. 4, 2016	Feb. 18, 2017	Apr. 24, 2017	Apr. 24, 2017
End date	May 18, 2022	May 23, 2022	Jun. 21, 2022	May 4, 2022
Sub-swath	1, 2	1, 2, 3	1, 2, 3	1, 2
Incidence angle ^a (°)	33.9, 39.3	33.9, 39.3, 43.9	33.9, 39.3, 43.9	33.9, 39.3

^a Each incline angle corresponds to a specific sub-swath image in a SAR data collection.

of the supplementary file. The distribution and coverage of each subswath SAR images are depicted as a corresponding polygon in Fig. 1. These polygons collectively encompass a total area of 111,066 square kilometers.

2.3. GNSS

The 24-hour continuous observations at cGNSS stations possess the ability to deliver static positioning results with a reliable millimeter-level accuracy (Bertiger et al., 2020), which were considered as ground-truth measurements for surface land motion monitoring. Daily vertical displacements processed by static point precise positioning (PPP) technique (Bertiger et al., 2020) were utilized to calibrate self-consistent InSAR results in each set of sub-swath images and validate the reliability of the final land deformation map. For this objective, PPP solutions processed by the GipsyX software suite were acquired for a total of 115 cGNSS stations as shown in Table S2 in the supplementary file (Blewitt

et al., 2018). These stations were selected to spatially overlap with SAR image coverage and to temporally overlap with InSAR time series for a period exceeding two years.

2.4. Hydrocarbon production

To examine the relationship between land deformation and oil/gas extraction, time series data of hydrocarbon production were obtained on a well-by-well basis from the Railroad Commission (RRC) of Texas. Specifically, each American Petroleum Institute (API) number, a unique number assigned to every oil and gas wellbores (RRC, 2023), with geographical coordinates provided by the RRC is considered as an independent wellbore for calculating hydrocarbon production at a particular location. The RRC of Texas recorded production data for each lease number in a particular district, which typically includes tens of counties. When calculating the hydrocarbon production for a specific API number, it is essential to consider the following key aspects (RRC,

2023): (1) An API number can be associated with multiple oil and/or gas leases, (2) Liquid hydrocarbons, referred to as condensate, can be isolated and extracted from natural gas wells, and (3) Gas can be naturally present in oil reservoirs or produced concurrently with the extraction of oil, commonly known as casinghead gas (RRC, 2023). As shown in Eq. (1), the API total production of gas, P_{gas}^{api} , was obtained from within the affiliated gas and oil leases. Similarly, the API total production of oil, P_{oil}^{api} , was calculated using oil and condensate data.

$$\begin{cases} P_{gas}^{api}(t) = \sum_{i=1}^{L} P_{gas}(t, l_i) + \sum_{j=1}^{M} P_{cas}(t, m_j) \\ P_{oil}^{api}(t) = \sum_{i=1}^{L} P_{con}(t, l_i) + \sum_{j=1}^{M} P_{oil}(t, m_j) \end{cases}$$
(1)

In Eq. (1), the sets of $\{l_1, l_2, \dots, l_L\}$ and $\{m_1, m_2, \dots, m_M\}$ represent gas and oil leases, respectively, which are associated with a particular API number. The variables P_{cas} and P_{con} represent the production of casinghead gas obtained from oil leases and condensate associated with gas leases, respectively. The production was measured in thousand cubic feet (MCF) for P_{gas}^{api} and barrels (BBL) for P_{oil}^{api} (RRC, 2023). And t denotes time in a per monthly interval after January 1, 2015. It is important to note that each gas lease corresponds to only one API number, whereas an oil lease may be associated with multiple wellbores (RRC, 2023).

2.5. Groundwater level observations

This study incorporated the dataset of groundwater-level altitude changes over the Houston-Galveston area (Ramage and Braun, 2022) to uncover the potential tie between observed land subsidence and groundwater consumption. The dataset was derived from groundwater-level observations stored in the National Water Information System (NWIS) (USGS, 2023), produced by the U.S. Geological Survey (USGS) in collaboration with local stakeholders. This study utilized long-term groundwater-level changes between 1990 and 2021 in the Chicot and Evangeline aquifers within the Houston-Galveston area. For the purpose of time series analysis, additional groundwater-level observations were accessed at the well level, sourced from both the USGS (USGS, 2023) and the Texas Water Development Board (TWDB) (TWDB, 2023), contingent upon data availability.

2.6. Croplands

In this study, we utilized cropland data, specifically the Landsat-derived global rainfed and irrigated-cropland product (LGRIP) (Teluguntla et al., 2023), to assess the association between the observed land subsidence and potential GW for irrigation purposes. The LGRIP product was generated by analyzing Landsat 8 data from 2014 to 2017. By considering spectral features and time-series characteristics, each 30 m grid cell was classified into distinct categories, including ocean, noncropland, rainfed cropland, and irrigated cropland (Teluguntla et al., 2023). The category of irrigated cropland was primarily employed to analyze the relationship between subsidence and irrigation.

2.7. Nighttime radiance data

Many anthropogenic activities that may induce land deformation involve continuous field work and maintenance, including activities related to routine oil and gas operations such as extraction and flaring at night. Thus, nighttime radiance vs. subsidence was investigated to explore the potential linkage. In this study, the day/night Band (DNB) data captured by the Visible Infrared Imaging Radiometer Suite (VIIRS) radiometer was utilized to enhance the understanding of HE activities in certain oil fields. Specifically, the cloud-free radiance of VIIRS DNB images between January 1, 2017, and January 1, 2022, was averaged using the Google Earth Engine (GEE) cloud computing platform (Elvidge et al., 2021). The spatial resolution of the VIIRS DNB data is around 500 m.

2.8. Sea surface height

To assess the risks of flooding stemming from land subsidence in the context of global sea-level rise, this study incorporated sea surface height (SSH) data for the ASLR variable. Specifically, long-term monthly sea-level anomalies spanning from January, 1993, to December, 2022, were acquired from the Copernicus Climate Change Service (C3S) (Copernicus Climate Change Service, Climate Data Store, 2018). The C3S SSH dataset is distinguished by its long-term stability, ensuring a reliable trend estimate, and boasts a spatial resolution of 0.25° by 0.25°. To mitigate signal degradation within altimeter footprints situated in regions where land and water intersect (Qiao et al., 2023), SSH grids that had their centers positioned in close proximity to shorelines were adopted, as illustrated in Figure S1 (i.e., the black dots) in the supplementary file. The Hector software was employed to estimate the ASLR trend of SSH time series. Hector incorporates an optimal noise model, effectively accounting for the influences of outliers, seasonality, and the step effect as outlined in previous works (Bos et al., 2013; Qiao et al., 2023).

3. Methods

3.1. PSI principle

Assuming a stack of N differential interferograms in relation to a common master acquisition, the differential phase $\phi(x,t_i)$ can be represented as:

$$\phi(x,t_i) = \varepsilon_{topo}(x,t_i) + d(x,t_i) + \alpha(x,t_i) + n(x,t_i). \tag{2}$$

In Eq. (2), t_i represents the temporal baseline of the ith interferogram. $\varepsilon_{topo}(x,t_i)$ represents the phase contribution proportional to both DEM error (i.e., $\varepsilon(x)$) and the geometrical baseline component (i.e., $B_n(t_i)$) perpendicular to the line-of-sight (LOS) direction, and thus $\varepsilon_{topo}(x,t_i)$ = $K_{\varepsilon} \cdot \varepsilon(x) \cdot B_n(t_i)$ holds with K_{ε} being a constant (Ferretti et al., 2000; Colesanti et al., 2003). $d(x, t_i)$ denotes the phase component attributable to LOS deformation of targets during the period of t_i and can be written as $\frac{4\pi}{r} \cdot v(x) \cdot t_i$ if a constant deformation rate of v(x) is assumed for the measurement wavelength λ . Lastly, $\alpha(x,t_i)$ represents the atmospheric phase contribution, and $n(x, t_i)$ accounts for the noise caused by decorrelation (Ferretti et al., 2001). The PSI technique was developed to isolate these phase contributions that are observed at point-like PS targets, which are characterized by low $n(x, t_i)$ values (Ferretti et al., 2000, 2001). PS candidates (PSCs) with low amplitude dispersion are assumed high coherent targets and selected as starting point to solve the system. Based on Eq. (2), differential calculations are then carried out between pairs of nearby PSCs (e.g., a connection within 2-3 km between x_1 and x_2 in a Delaunay triangulation):

$$\Delta\phi(x_1, x_2, t_i) = K_{\varepsilon} \cdot \Delta\varepsilon(x_1, x_2) \cdot B_n(t_i) + \frac{4\pi}{\lambda} \cdot \Delta v(x_1, x_2) \cdot t_i$$

$$+ \Delta w(x_1, x_2, t_i)$$
(3)

where $\Delta w(x,t_i)$ refers to the differential phase residual between the paired PSCs that includes differential contributions of $\Delta\alpha(x_1, x_2, t_i)$, $\Delta n(x_1, x_2, t_i)$, and possible temporal non-linear deformation (Ferretti et al., 2000; Colesanti et al., 2003). By jointly estimating $\Delta \varepsilon(x_1, x_2)$ and $\Delta v(x_1, x_2)$ using spectral analysis, it becomes possible to unwrap $\Delta \phi(x_1, x_2, t_i)$ and integrate it along a path within the network, which results in the derivation of an unwrapped interferogram for $\phi(x,t_i)$ (Ferresults in the derivation of an unwrapped interferogram for $\phi(x,t_i)$ retti et al., 2000; Colesanti et al., 2003). Then with $\Delta \varepsilon$ and Δv integrated, the atmospheric phase screen (APS) contribution at PSCs can be isolated and utilized for estimating atmospheric phase delay at regular grids through interpolation given its low-wavelength characteristics (Colesanti et al., 2003; Kampes, 2014). It should be noted that the APS estimate is the sum of tropospheric effects such as turbulence and stratification phenomenon and ionospheric effects (Ferretti, 2014). To incorporate more PS targets, ε and v are jointly estimated again through phase analysis, following the removal of estimated APS from $\phi(x, t_i)$. More details about the PSI technique can be found in the relevant Refs. (Ferretti et al., 2000, 2001; Colesanti et al., 2003; Kampes, 2014).

3.2. PSI processing

As outlined in Procedure 1, the LOS land deformation for each stack of sub-swath SAR images was computed by undergoing a series of key stages, including pre-processing, preparation, APS estimation, and PS processing. During pre-processing, the stacked images in VV polarization were initially cropped to cover the land near the Texas Gulf Coast and are subsequently co-registered with selected master imagery. In the data preparation stage, the amplitude stability index (ASI) was calculated for each pixel using the standard deviation (σ_A) and the mean (m_A) of the amplitude values, where ASI is defined as ASI = 1 $\frac{\sigma_A}{r}$. To derive the differential interferometric phases, 90 m-resolution DEM from the Shuttle Radar Topography Mission (SRTM) was used and resampled to the SAR coordinates. Additionally, a ground control point (GCP) was employed to ensure accurate geocoding. Moving forward to the next stage the APS was separated by jointly estimating DEM errors and deformation velocity through the spatial connections of a Delaunay triangulation which was created using selected PSCs with $ASI > t_1$. And in the final stage, the phase measurements were analyzed again after APS removal to reliably estimate the residual height and velocity of land deformation for a larger number of PS targets selected by $ASI > t_2$. The thresholds t_1 and t_2 were used to select stable PS targets that were used for both APS estimate and land deformation estimate. The PSI processing routines were performed in the SARPROZ software (Perissin et al., 2011; SARPROZ, 2023).

Procedure 1: PSI Data Processing

Data: Sentinel-1 SLC, SRTM DEM, and precise orbit ephemerides (POE)

Pre-processing:

- 1) Choose sub-swath and apply POE
- 2) Select master imagery and subset area
- 3) Extract and co-register SAR data

Preparation:

- 4) Calculate amplitude stability index (ASI)
- 5) Select DEM and re-sample it to SAR coordinates
- 6) Select a GCP for geocoding

APS Estimate:

- **7)** Select PSCs with $ASI > t_1$
- 8) Create a spatial graph
- 9) Process network connections
- 10) Select a reference point
- 11) Estimate APS

PS Processing:

- 12) Select PSs with $ASI > t_2$
- 13) Analyze phases of PSs after APS removal

Result: Coordinates of PSs, displacement time series, deformation velocity, and temporal coherence.

3.3. InSAR result calibration and validation

Measurements of cGNSS stations were used to calibrate the subswath InSAR results and validate the regional VLM map. The calibration was performed to accurately align the self-consistent InSAR VLM results with the vertical components of cGNSS measurements. In addition, the individual VLM map segments, each stemming from an employed set of sub-swath images (Table 1) and providing only partial coverage of the study area of interest. It is worth noting that interruptions to cGNSS observations were occasionally observed at some stations, which caused the PPP solutions in the vertical direction to be vertically shifted into segments due to factors such as antenna changes, natural disasters, and other unexpected interventions. The Hector software was utilized to estimate the trend of cGNSS solutions in the vertical direction.

By combining three LOS velocities acquired from different SAR looking directions, it is possible to decompose the land deformation

at a specific location into both horizontal components of the East-West and North-South directions and vertical deformation (Hu et al., 2014). However, in practical applications, the North-South land deformation is typically neglected when using Sentinel-1 InSAR due to its near-polar orbit radiation (Cigna et al., 2021). In this study, the ascending LOS results were converted to the vertical direction using the formula $V_{\mu} = (\cos\theta)^{-1}V_{LOS}$ by further neglecting the East-West contribution (Tay et al., 2022). Furthermore, given that InSAR results are inherently self-consistent with respect to the selected date and spatial reference point, PSI velocity results were vertically calibrated by employing observations from two cGNSS stations within each subswath scene. This calibration involved the utilization of data from two selected cGNSS stations. Subsequently, the calibrated results from all sub-swath data were merged to generate a comprehensive subsidence map covering the entire study area. Specifically, Eq. (4) was employed for converting the LOS measurements into vertical direction and for calibrating subsidence velocity across the sub-swath processing results, as previously mentioned.

$$V_u = \frac{1}{\cos\theta} V_{LOS} + b \tag{4}$$

where θ is the average incline angle of the specific sub-swath imagery, and b is a mean vertical velocity difference between each of cGNSS station and a cluster of PS points within their 100 m buffer zone around the station. For validation purposes, the remaining cGNSS stations within each set of sub-swath images were utilized to quantitatively evaluate the performance of the calibrated and merged land deformation map.

4. Results

4.1. Land deformation map

Each set of sub-swath images was processed by following steps in Procedure 1. A master image chosen for each sub-swath data was positioned near the center of the spatial and temporal baseline distribution. During the APS estimation stage in Procedure 1, the default threshold value for t_1 was set at 0.75. However, for certain sub-swath extent covering rural areas, t_1 was adjusted to lower values (e.g., 0.6 or 0.65). This adjustment ensured the inclusion of a sufficient number of PSCs and yielded a reliable APS estimate. To select a reference point, a PSC target was chosen based on high phase coherence and an average value of $\Delta \varepsilon(x_1, x_2)$ close to zero. For each sub-swath processing, the threshold value for t_2 was set lower than t_1 , ranging from 0.65 to 0.55. The specific value of t_2 depended on the primary land-cover types, whether rural or urban. Only PSs with coherence values exceeding 0.4 were exported for land deformation estimation. Additional information on sub-swath data processing can be found in Table S3 of the supplementary file.

The LOS PSI results across different sub-swath images were calibrated as per Eq. (4) to obtain the regional land-deformation map along the Texas Coast. Specifically, in each set of sub-swath images, the corresponding incidence angle from Table 1 was utilized to project the LOS deformation into vertical direction. Shifts to cGNSS time series due to events such as earthquakes and antenna code changes (Blewitt et al., 2018), were taken into account for reliable trend estimation in Hector. Only GNSS observations recorded between January 1, 2017, and January 1, 2022, were considered and a total of 115 cGNSS stations were included in the study for calibration and validation purposes, provided they had observation records spanning a total of over two years and contained at least one PS target within the 100 m buffer zone. Selected cGNSS stations in each set of SAR sub-swath images for velocity calibration were featured by wide spatial distribution and shift-free observation history in long time series.

The accuracy of the calibrated land deformation map was validated through a comparison between InSAR and GNSS measurements. The scatter plot in Fig. 2 demonstrates a favorable overall agreement

 Table 2

 Overview of attribution of subsidence hotspots

Name	Location in Texas	Prior studies attributed VLM to	Supporting results in this study ¹	
H01	McAllen	HE (Qu et al., 2023)	Localized and asymmetric bowl-shaped patterns towards the East can be observed in both deformation and HE in Fig. 5(a)–(b).	
H02	Hidalgo County	HE (Qu et al., 2023)	In Fig. 5(c)-(d), numerous oil/gas wells aligning with PS targets (e.g., the pumpjack) in the rural areas suggest linkage between the VLM and HE.	
H03	Premont	HE (Qu et al., 2023)	The presence and production of oil/gas wells (Fig. 5(e)–(f)) and the declining groundwater levels at various sites (Figure S3(c)) suggest a mixed factors contributing to the VLM, including HE and GW.	
H04	Corpus Christi	HE (Ratzlaff, 1982; Haley et al., 2022; Qu et al., 2023)	The presence and productivity of oil/gas wells (Fig. 5(g)–(h)) suggest the correlation between deformation and HE activities.	
H05	Refugio	HE (Ratzlaff, 1982)	The VLM may be attributed to HE near Refugio, TX, (Fig. 5(i)–(j)) and probable GW near Victoria, TX, (Younas et al., 2022) as evidenced at wells 7924702, 7924102, and 7923601 (Figure S3(d)).	
H06-07	Karnes City and Shiner	HE (Haley et al., 2022)	Data of hydrocarbon and nighttime light revealed strong coincidence between subsidence and HE activities (Fig. 5(k)–(m)). Nighttime radiance is believed to originate from drilling operations, oil/gas infrastructures, and gas flares of HE activities.	
H08	Freeport	GW and salt dome movements (Ratzlaff, 1982; Zhou et al., 2021; Qu et al., 2015)	Peak VLM velocities near the Stratton Ridge salt dome (Fig. 6) and groundwater levels dropping during the early 2000s (Figure S5) suggest the linkage between the VLM and salt dome movement and industrial activities.	
H09	Liverpool	-	The combined factors of HE, cropland irrigation (Fig. 6), and groundwater level declines between 2008 and 2015 (Figure S6) may explain VLM.	
H10	Manvel	-	Spatial coincidence between GW and the VLM is observed in Fig. 6.	
H11-12	Katy and Woodlands	GW (Qu et al., 2015; Khan et al., 2022; Liu et al., 2022)	Significant changes in groundwater levels (Fig. 6) and probably minor impacts from HE (Fig. 4) may contribute to the VLM.	
H13 H14	Channelview Mont Belvieu	HE (Qu and Lu, 2022) HE (Qu et al., 2015; Liu et al., 2022)	HE and inconspicuous GW activities are observed in Fig. 6. The VLM is attributed to HE and probably GW for municipal and industry purposes (Fig. 6).	
H15	Stowell	_	HE and possible GW for irrigation (Fig. 7) may explain the VLM.	
H16 H17	Beaumont Beaumont	HE and GW (Qu et al., 2023) HE and sulfur mining (Ratzlaff, 1982)	HE and possible GW for irrigation (Fig. 7) may explain the VLM. Fig. 7 shows association between the localized subsidence pattern and HE activities.	
H18	Vidor	-	The VLM is probably caused by HE as shown in Fig. 7.	
H19	Orange	_	The VLM is probably caused by HE as shown in Fig. 7.	

^{1.} Figures and Tables stating with letter S can be found in the supplementary file.

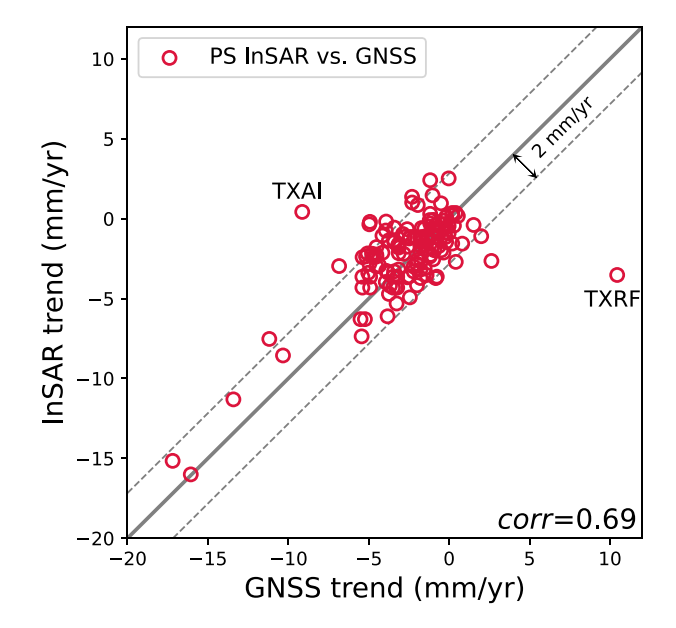


Fig. 2. Comparison of trends between GNSS velocity and average land deformation derived from PS targets within a 100 m buffer zone around each cGNSS station. The solid line represents perfect agreement, while the dashed lines depict the upper and lower bounds of 2.0 mm/yr for visualization purposes. The correlation coefficient is denoted as *corr*.

between the two space-borne geodetic techniques, with a correlation coefficient reaching up to 0.69. The average velocity difference of land deformation between PS points and cGNSS stations was -0.35 mm/yr, and a mean absolute deviation (MAD) equated to 1.60 mm/yr. However, it is essential to recognize that various factors may account for the discrepancies in subsidence velocity between cGNSS and InSAR results. These factors include: (1) the spatial variability of subsidence between a cGNSS station and its nearby PS targets, and (2) the limited observation length of some cGNSS stations. Figure S2 of the supplementary displays an example at the TXRF cGNSS station that its observation history was limited, potentially affecting the VLM trend estimation (Fig. 2.)

Fig. 3 illustrates the velocity results of land deformation with over 1.7 million PS targets. The calibrated and merged land deformation map appears generally smooth over space, though there is a noticeable stripe effect between the "34_90_1" and "34_90_2" sub-swath images, where densely distributed croplands can be observed from the upper inset map shown in Fig. 3. Lush vegetation in the terrain likely led to a decrease in the number of PS targets between the "34_90_1" and "34_90_2" sub-swath images, thereby inducing errors in phase unwrapping (Ferretti, 2014). By analyzing both Fig. 2 and Fig. 3, it is evident that an overall rate of land subsidence across the Texas coastal areas fell within the range of ±5 mm/yr. However, localized deformation hotspots were documented, e.g., the five stations with GNSS subsidence trends exceeding -10.0 mm/yr, Fig. 2. It is important to highlight that the PSI results provide valuable insights into the spatial patterns and variability of land deformation, which is not easily discernible with the sparsely distributed cGNSS stations. In Fig. 3, 19 subsidence hotspots are identified and marked as pink boxes, ranging from "H01" to "H19". However, it should be noted that the deformation areas situated at the intersection between the "34_90_1" and "34_90_2" sub-swath images

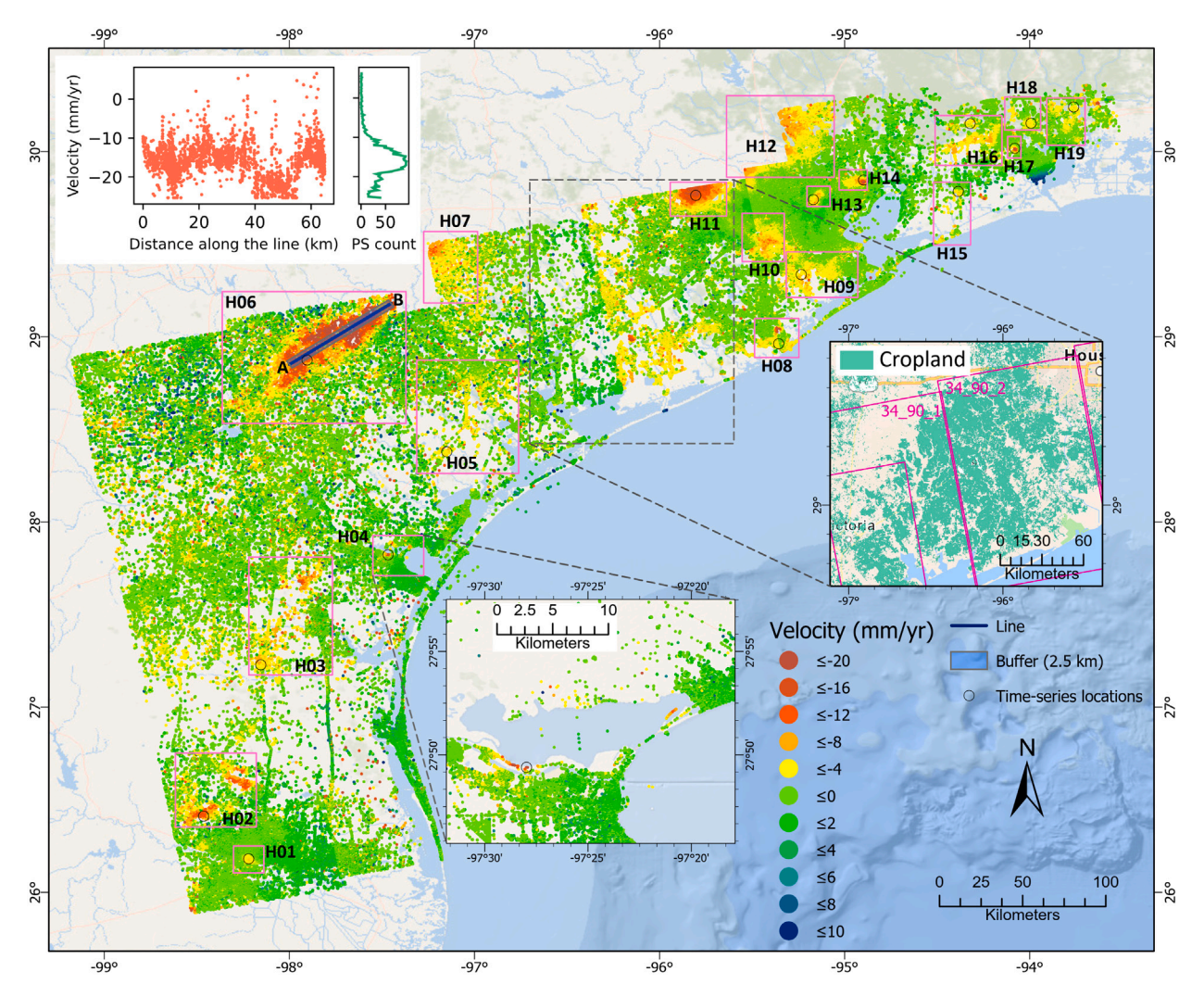


Fig. 3. Map of land deformation velocity along the Texas Coast. The pink rectangles indicate some subsidence hotspots, numbered from 'H01' to 'H19' across the entire study region. The lower inset map highlights the hotspot at H04, while the upper inset map displays both irrigated and rainfed croplands, located near the stripe between '34_90_1' and '34_90_2' sub-swath images. The upper-left corner of the map features the profile (from A to B) and histogram, illustrating the subsidence and its distribution of PS targets within the buffer zone encompassing the hotspot H06. (For interpretation of the references to color in this figure legend, the reader is referred to the web version of this article.)

Source: Cropland data adapted from Teluguntla et al. (2023).

were not designated as hotspots, primarily due to the potential interference from stripe effect. Subsidence patterns near the Houston-Galveston Area in this study were also echoed by prior studies (Liu et al., 2022; Khan et al., 2022), for example near Katy, TX, as the hotspot H11 shows in Fig. 3.

4.2. Attribution of land subsidence

This study examined the relationship between land subsidence and various potential linking factors, including changes in groundwater levels, the location and production of oil/gas wells, distribution of cropland and salt domes, as well as DNB observations. The 19 hotspots depicted in Fig. 3 were segmented into three distinct regions for analysis, including: H01–H07 in the Coastal Bend and South Texas (Fig. 5), H08–H14 in the Houston-Galveston Area (Fig. 6), and H15–H19 in the Southeast Texas (Fig. 7). A summary of the analyses conducted on each of these 19 identified subsidence hotspots is presented in Table 2. Hotspots H06 and H07 were treated collectively in Table 2, assuming their association with an extended area governed by similar subsidence drivers. The same was applied to hotspots H11 and H12. Table 2 outlines potential drivers linked to these subsidence hotspots, as documented by previous studies, and presents results derived from this study. Besides, Fig. 4 provides a time series comparison

among cGNSS/InSAR displacements, groundwater levels, and hydrocarbon production collected in the proximity of the circle markers shown in Fig. 3. Hotspots of H07 and H12 are excluded from the time series analysis in Fig. 4 since they were integrated into H06 and H11, respectively. H10 is not shown in Fig. 4 due to the unavailability of time-series data for both HE and GW during the study period. In addition to the attribution analysis at individual hotspots, the following conclusions were drawn:

- (1) In the Coastal Bend and South Texas region, the primary driver of subsidence is believed to be HE activities. Moreover, in this region, land subsidence attributed to GW for irrigation purposes appears to be minor, as indicated by the non-overlapping distribution of croplands in the subsidence maps (see Figure S4 in the supplementary file). Nonetheless, further analysis is warranted to investigate subsidence attribution at H03 and H05.
- (2) Within the Houston-Galveston Area, land subsidence is attributed to a combination of multiple factors, including GW, HE, and the presence of salt domes. Subsidence linked to GW at hotspots H11 and H12 has been extensively documented in previous studies (Galloway et al., 1999; Qu et al., 2015, 2023; Liu et al., 2022; Khan et al., 2022). As evident from the H11 subplot in Fig. 4, groundwater levels exhibited a continuous decline

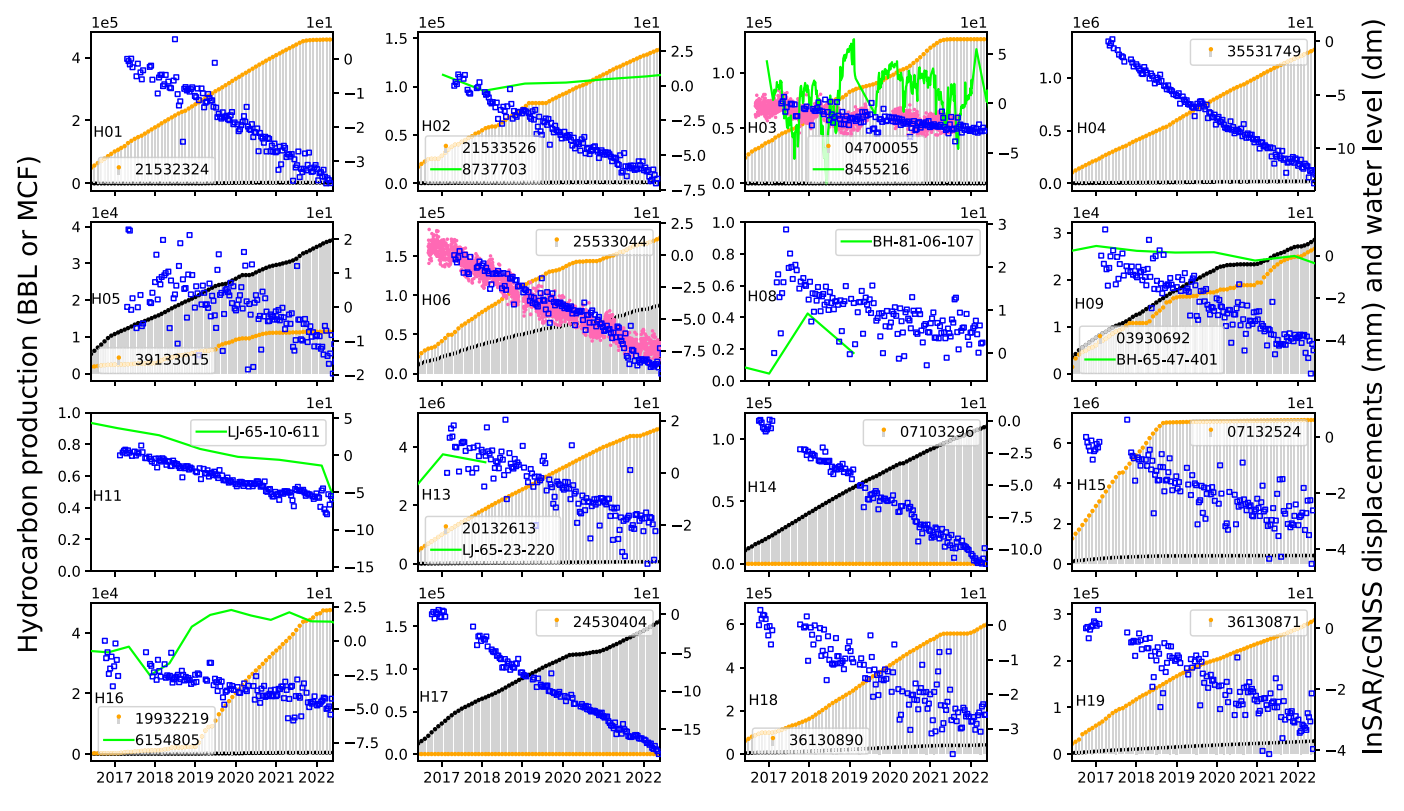


Fig. 4. For hotspots marked with black open circles in Fig. 3, time series of multi-source data collected near the circle are compared, including displacements observed at cGNSS stations (pink dots for TXFF at H03 and TXKC at H06) and InSAR PS points (blue squares), cumulative hydrocarbon production starting from January 2016 (black bars for BBL and orange for MCF for the same API wellbore calculated with Eq. (1)), and groundwater elevations (green solid line). To enhance visualization, water level data in each subplot were transformed from their original meter values above sea level to decimeters (dm) after subtracting the mean sea level of the entire time series. Additionally, the hydrocarbon API and groundwater well ID are specified within each subplot. Groundwater level observations were sourced from USGS for hotspots H08–H13 and from the TWDB for the remaining hotspots. (For interpretation of the references to color in this figure legend, the reader is referred to the web version of this article.)

throughout the study period. The localized subsidence patterns observed at H13 and H14 are highly indicative of being caused by HE activities. Additionally, hotspot H10 may also be influenced by GW, given its spatial coincidence with subsidence. On the other hand, subsidence drivers for hotspots H08 and H09 appear to be complex and may require further investigations for a comprehensive understanding.

(3) In general, it is believed that land subsidence hotspots in the Southeast Texas region, ranging from H15 to H19, are commonly associated with HE activities. While GW, primarily for irrigation practices and municipal water usage, could potentially contribute to land subsidence at certain hotspots in this region (Qu et al., 2023), its impacts on current land subsidence in Southeast Texas are considered minor. This assessment is supported by the overall rising trend of water levels, as illustrated in Figure S7 in the supplementary file.

4.3. Land subsidence near the Texas shorelines

In this study, particular emphasis was placed on investigating land subsidence near the shorelines of Texas. To account for the uneven distribution of PS points and facilitate coastal subsidence-related planning and decision-making for pertinent stakeholders, spatial grids were employed to delineate and quantify land subsidence along the shorelines within the study area. To accomplish this, continuous square polygons measuring 500 m by 500 m were initially generated, aligning with the spatial coverage of SAR images. The velocities of PS points within each grid were then averaged to represent the land deformation for the corresponding grid cell. Additionally, the distance of each grid cell to the shorelines was calculated. Results indicate that the

entire study area is experiencing subsidence at an average velocity of -2.6 mm/yr. However, grid cells located within 50 km of the Texas shorelines exhibit an average subsidence rate of -2.1 mm/yr, as depicted in Fig. 8(a). Fig. 8(b) provides a more detailed representation of subsidence variations away from the coastlines:

- (1). A substantial number of grids are distributed within 10 km of the shorelines, as depicted in Fig. 8(b), facilitating the monitoring VLM for both coastal residents and infrastructures along the Texas coastline. It is worth noting that PS points primarily comprise man-made objects such as buildings, metallic structures, and urban infrastructures (Ferretti, 2014).
- (2). The VLM rates of the densely populated grids exhibit variations ranging from approximately -5.0 mm/yr to 1.0 mm/yr, aligning with the velocity range observed in Fig. 2 for cGNSS measurements.
- (3). The subsidence rates of grid cells located near the Texas coastlines converge toward -1.0 mm/yr. This finding aligns with the subsidence trend of -1.4 mm/yr reported in a prior study that employed data from TG and cGNSS stations (Zhou et al., 2021).
- (4). The extent of subsidence exhibits an escalating trend as the distance of the grids from the shorelines increase. This phenomenon is likely attributed to the heightened intensity of anthropogenic activities farther away from the coastlines.
- (5). A considerable number of shoreline grids exhibit subsidence rates exceeding 3.0 mm/yr, a magnitude equivalent to the reported global sea-level rise rate between 1993 and 2014 (Chen et al., 2017). It becomes imperative to estimate the RSLR in order to assess the likelihood of high-tide and storm-related flooding risks, in the context of rising sea levels in relation to subsiding land along the Texas Gulf Coast.

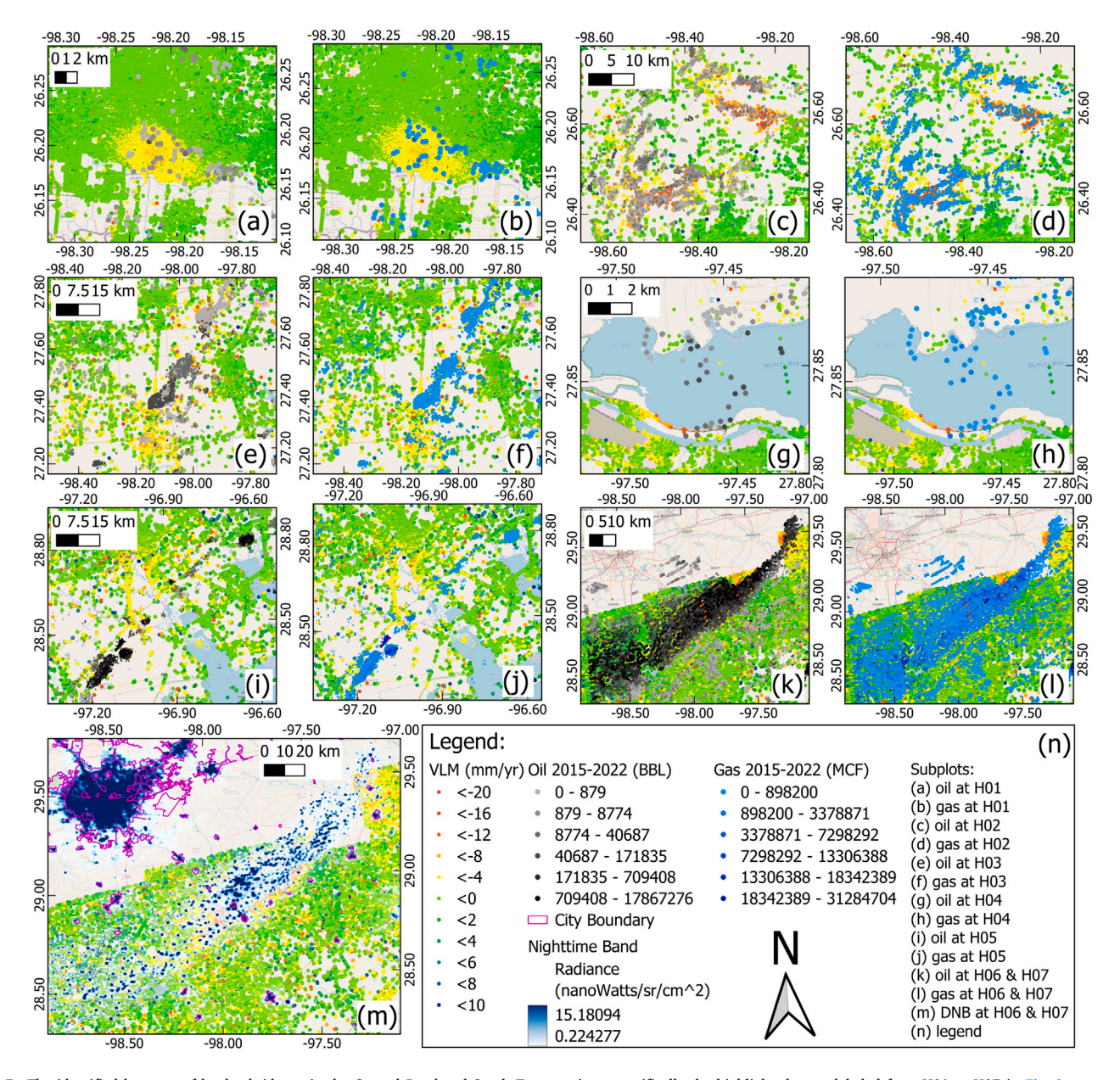


Fig. 5. The identified hotspots of land subsidence in the Coastal Bend and South Texas regions, specifically the highlighted areas labeled from H01 to H07 in Fig. 3, are overlaid with observations of hydrocarbon production and the DNB. Subplots (a)–(l) present the cumulative hydrocarbon production from 2015 to 2022, calculated using Eq. (1), while subplot (m) focuses specifically on H06 and H07, illustrating the average radiance of the DNB between 2017 and 2021. The symbol size representing oil and gas production was adjusted as needed for optimal clarity.

4.4. Coastal flooding risks

To select grids located near the shorelines, a buffer zone of 250 m was created on each side of the shorelines, and only the grid cells that intersected with the shoreline buffer zone were utilized for analysis, referred to as shoreline grids. It is important to note that shoreline grids with fewer than five PS targets were excluded from the analysis to ensure reliability. Out of the initial grid dataset, a total of 1532 shoreline grids remained, encompassing 50,313 PS targets. Subsequently, the RSLR was computed at the grid level using the equation $v_{RSLR} = v_{VLM}$. To determine the RSLR of a specific shoreline grid, this calculation involved combining its VLM velocity with the ASLR trend of the proximity SSH footprint. The locations of SSH grid cells are visualized in Figure S1. In this study, the RSLR rate was employed to gauge potential flooding risks from subsidence and climate change. A higher RSLR rate indicates an increased likelihood of coastal flooding events during high-tide and storm days.

Fig. 9 visually presents the RSLR along the shorelines in grid format, offering valuable insights into flooding risks within the context of global sea-level rise and local subsidence. Overall, results of the study suggest around 6.0 mm/yr sea-level rise over the Texas coastlines (Fig. 9(i)), and this amount almost double of the global sea-level rise between 1993 and 2014. However, RLSR was also characterized with spatial variability due to coastal subsidence and some local areas were experiencing higher RSLR rates than 6.0 mm/yr. The RSLR spatial variability of selected areas can be observed in Fig. 9, where subplot (a) focuses on Padre Island, renowned as the world's longest undeveloped barrier island. Subplots (b) to (d) correspond to localized areas along the Coastal Bend and subplots (e) to (h) are associated with the Houston and its surrounding regions. Further examination of these flooding hotspots is detailed below:

Referring to Figure S1, it is evident that the barrier island exhibits general stability in terms of the VLM. However, notably

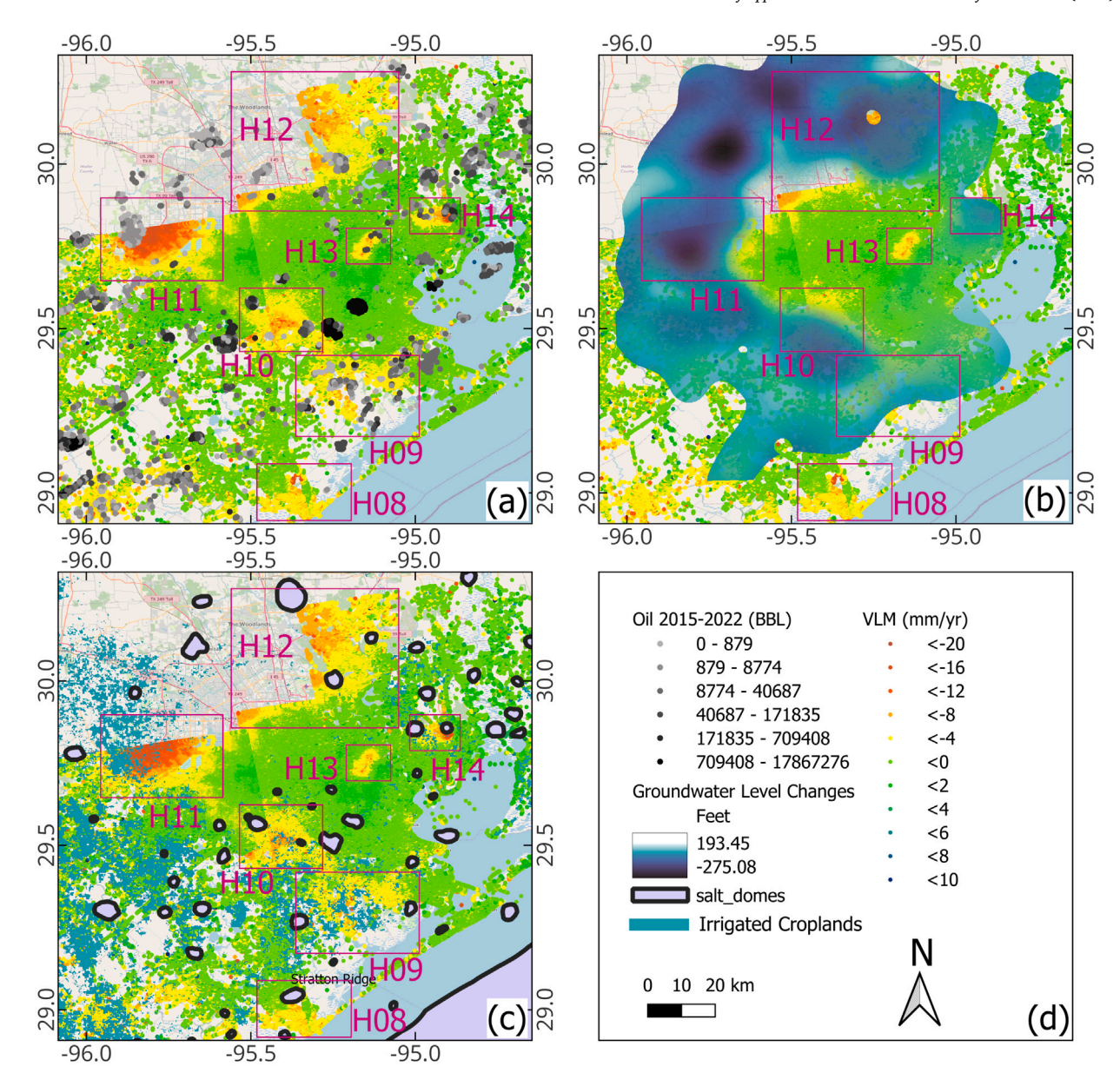


Fig. 6. Maps for attribution analysis at the Houston-Galveston region, examining the spatial relationship between land subsidence and three factors: (a) total oil production, (b) long-term groundwater altitude changes from 1990 to 2021 (Ramage and Braun, 2022), and (c) distribution of irrigated cropland and salt domes. Only pixels with negative values of groundwater level changes are shown in the subplot (b). The subplot (d) shows the legend.

high ASLR rates in the southern region of Padre Island significantly contribute to the observed spatial variability of the RSLR (Fig. 9(a)).

(2). Two noteworthy local RSLR hotspots were identified within the Texas Coastal Bend, specifically near Corpus Christi and Rockport (as depicted in Fig. 9(b) and (c)). The RSLR rate near Corpus Christi soared to 24.0 mm/yr, which is approximately eight times the magnitude of the global sea-level rise observed between 1993 and 2014. The substantial land subsidence observed in Corpus Christi is primarily attributed to oil and gas extraction, as discussed in Section 4.2. Near Rockport, some shoreline grids experienced up to 9 mm/yr RSLR. Prior measurements collected at both cGNSS and TG stations in the area have reported subsidence trends exceeding –4.0 mm/yr (Qiao et al., 2021, 2022, 2023). A comprehensive study is warranted to thoroughly analyze the long-term spatial–temporal variations in land subsidence near Rockport and ascertain their underlying causes.

(3). A total of five RSLR hotspots were identified in the vicinity of Houston and its surrounding areas, namely Freeport (Fig. 9(e)), Galveston Island (Fig. 9(f)), Bolivar Peninsula (Fig. 9(g)), Seabrook, and San Leon (Fig. 9(h)). Highlighted RSLR rates at these areas were mainly due to land subsidence. In the case of Freeport, prior studies have reported a land subsidence rate of approximately -2.0mm/year (Qiao et al., 2023; Zhou et al., 2021). However, it is worth noting that these stations are situated away from the shorelines and may not have fully captured the subsidence variability, as illustrated by the PSI estimates in the area (Fig. 9(e)).

5. Discussion

This section offers discussions encompassing the limitations, unexplored facets of subsidence attribution, and potential directions for future research, all rooted in the results and findings of this study. First, to enhance the precision of subsidence hotspot detection over

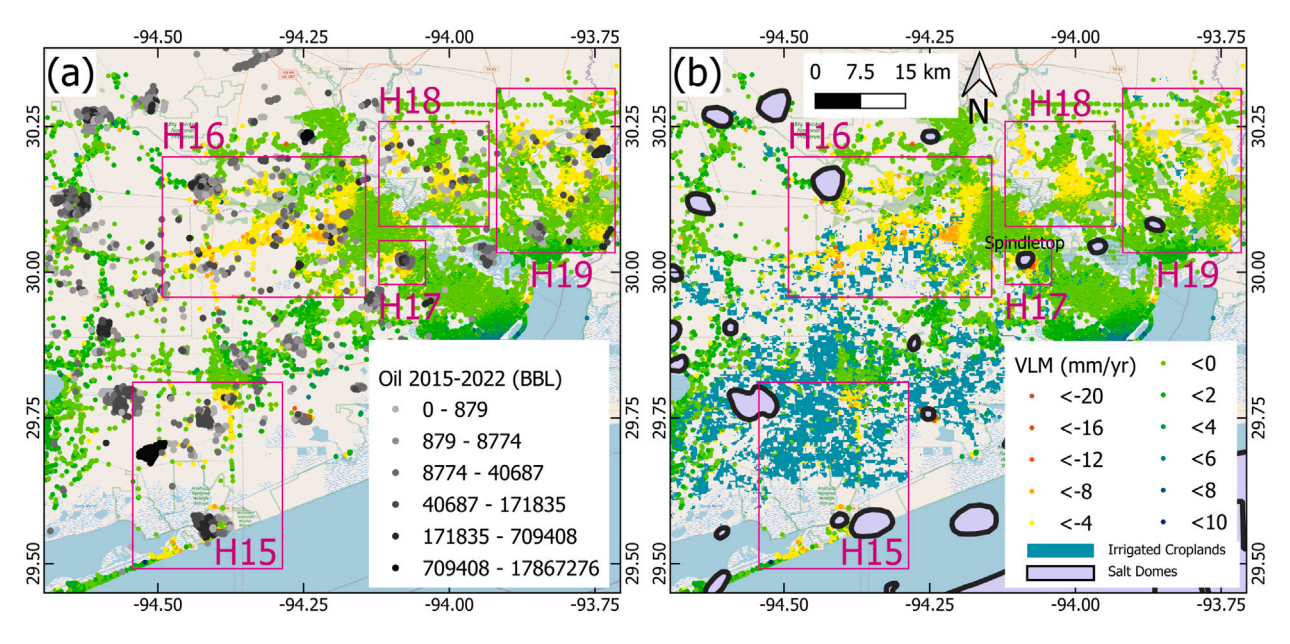


Fig. 7. Attribution analysis in the Southeast Texas region, comparing land subsidence with: (a) oil production, and (b) croplands and salt domes.

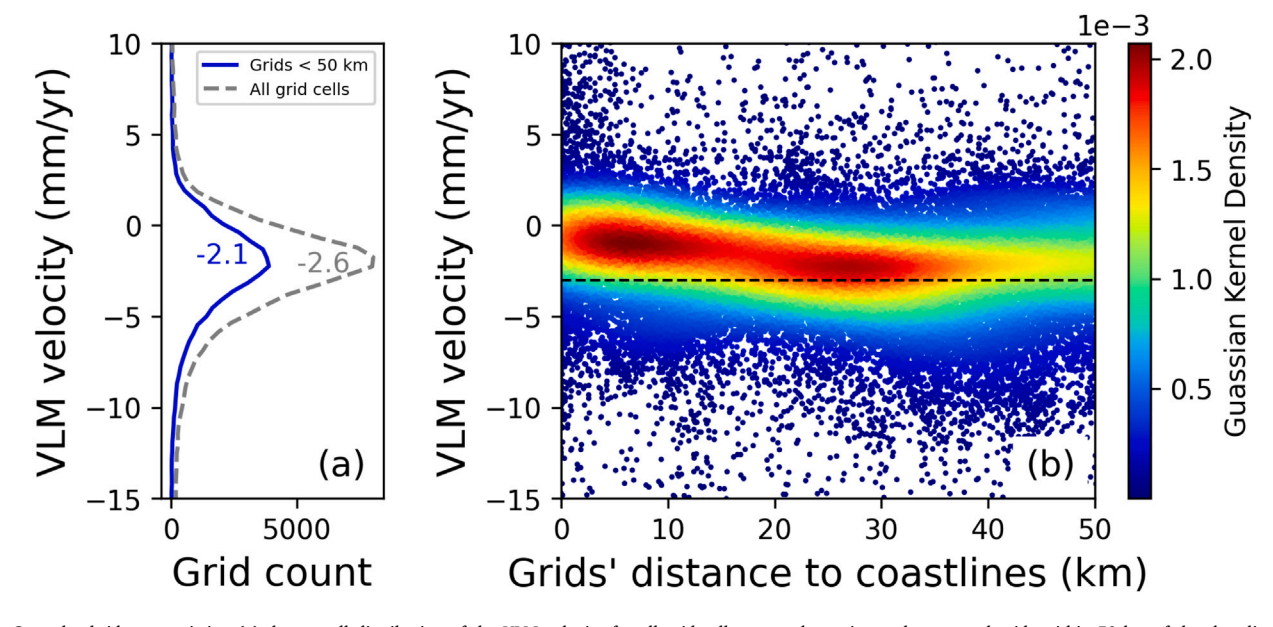


Fig. 8. Coastal subsidence statistics: (a) the overall distribution of the VLM velocity for all grid cells across the entire study area and grids within 50 km of the shorelines, along with the mean value indicated, and (b) the relationship between the VLM and the distance of grid cells to coastlines, with red indicating higher grid density estimated using Gaussian kernel. The dashed line in the subplot (b) at -3 mm/yr is for a comparison in magnitude to the global mean sea-level rise between 1993 and 2014 (Chen et al., 2017). (For interpretation of the references to color in this figure legend, the reader is referred to the web version of this article.)

a large-scale area, improvements in InSAR estimation can be pursued with a focus on the following aspects: (1) leveraging the small baseline subset (SBAS) InSAR method and using higher resolution DEM to incorporate low coherence pixels (Yunjun et al., 2019; Du et al., 2017), e.g., the masked SAR pixels evident in the PSI results of this study, to enhance spatial coverage; (2) employing advanced algorithms for reliable phase unwrapping and InSAR estimation (Huang and Biondi, 2023) in response to addressing challenges such as the stripe effect observed between '34_90_1' and '34_90_2' sub-swath data; and (3) utilizing varied inclination angles within sub-swath SAR imagery and incorporating both ascending and descending tracks to facilitate reliable InSAR estimates, for instance, in mitigating subtle inconsistencies between sub-swath data of '34_90_2' and '34_90_3' in this study (Xu et al., 2021).

In addition, while this study primarily focused on identifying the primary drivers associated with localized subsidence hotspots along the Texas Gulf Coast, it is important to acknowledge that other factors may also contribute to observed subsidence. For example, on a tectonic scale, subsidence can result from geological forces linked to tectonic plate movements, sediment compaction, the glacial isostatic adjustment (GIA), and the like (Zhou et al., 2021). Besides, geological faults and other subsurface geological features may spatially influence subsidence patterns (Castellazzi et al., 2016). Furthermore, as mentioned in Section 2.4, according to RRC (RRC, 2023), the released hydrocarbon production of a specific oil lease may link with multiple API numbers, which may amplify, to some extent, the estimates of hydrocarbon production at some locations. Furthermore, it is imperative to conduct additional investigations aimed at gathering subsurface observations and evidence linked to HE and GW activities. These investigations

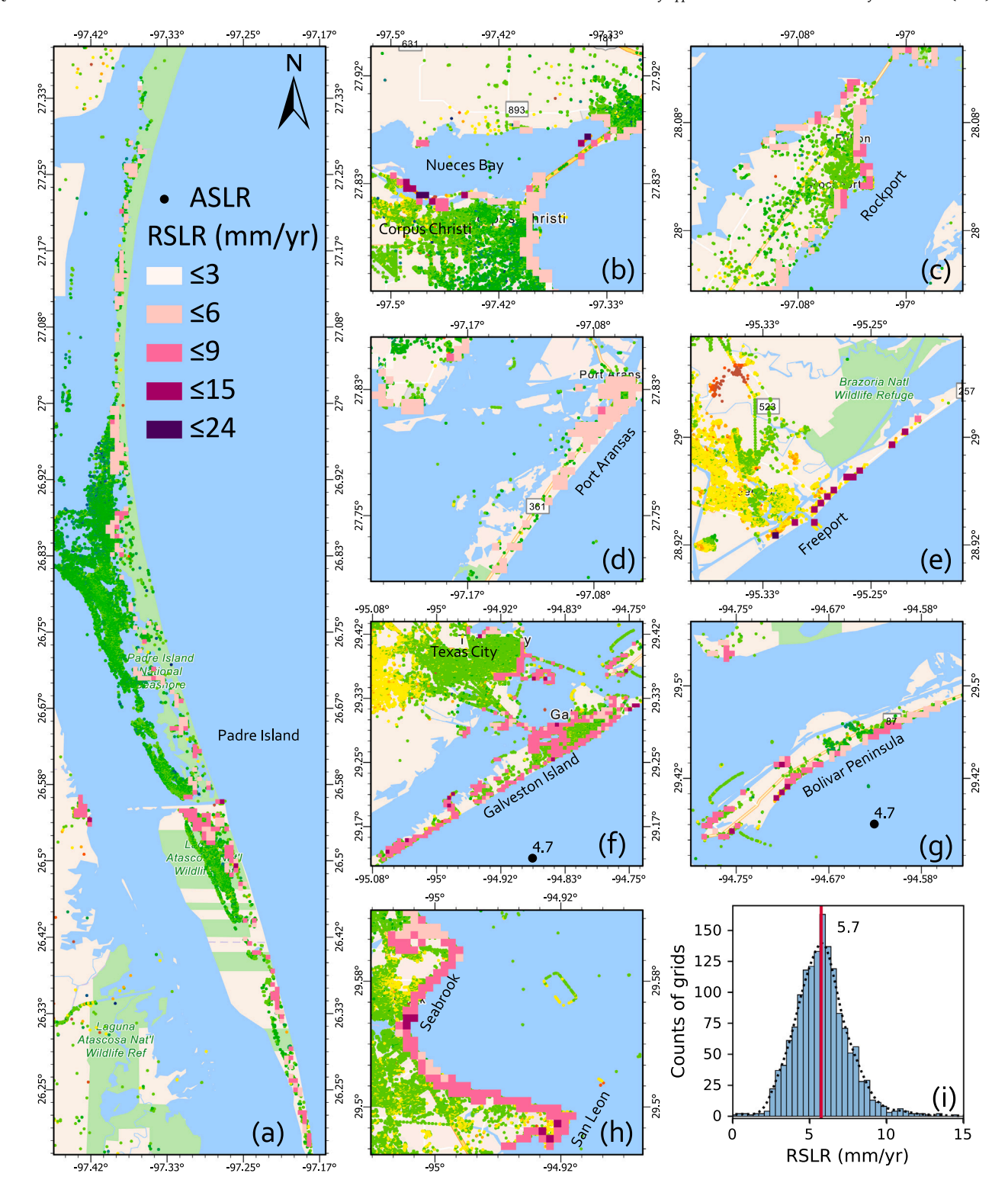


Fig. 9. Shoreline RSLR estimate in the form of grids overlapping with PSI results in specific local areas in Texas: (a) Padre Island, (b) Corpus Christi, (c) Rockport, (d) Port Aransas, (e) Freeport, (f) Galveston Island and Texas City, (g) Bolivar Peninsula, and (h) San Leon and Seabrook. Subplot (i) presents the distribution of all 1532 shoreline grids along the Texas coastlines, where the red vertical line represents mean value of RSLR estimates and the dashed line displays the best fitted curve. The same VLM velocity legend of PSs is employed as shown in Fig. 3. (For interpretation of the references to color in this figure legend, the reader is referred to the web version of this article.)

will help elucidate the observed land subsidence from a geological perspective, particularly for those hotspots where identifying the subsidence drivers has proven challenging. Examples of such hotspots in this study include H03, H05, H08, and H09. Finally, reliable prediction of the RSLR also depends on the accuracy of ASLR trend estimate,

which requires very long-term sea-level observations over 70 years or even longer period due to the decadal sea-level variability (Douglas et al., 2000). Addressing these aspects in future research endeavors is supposed to contribute to a more comprehensive understanding of land subsidence dynamics in the study area.

6. Conclusion

To create a large-scale regional land subsidence map near the Texas Gulf Coast, this study employed the PS InSAR technique to process Sentinel-1 SAR images from 2016 to 2022. The results from sub-swath InSAR imagery were projected into the vertical direction and combined to generate the regional subsidence map. Overall, the study successfully produced a smooth subsidence map for the area, except for a stripe effect observed between sub-swath images of '34_90_1' and '34_90_2'. The comparison of subsidence velocity revealed a strong agreement between InSAR and co-located cGNSS estimates, exhibiting a correlation coefficient of up to 0.69, an average velocity difference of -0.35 mm/yr, and a mean absolute deviation (MAD) of 1.60 mm/yr. The study identified a total of 19 subsiding hotspots and analyzed potential drivers associated with land subsidence. In the Coastal Bend and South Texas regions, land subsidence was strongly attributed to HE activities. In the Houston-Galveston area, both factors of groundwater withdrawal and oil/gas pumping are believed to contribute to land subsidence. Meanwhile, subsidence in Southeast Texas was likely mainly caused by HE, considering the relatively inconspicuous trend of dropping groundwater levels in the area. The statistics derived from the VLM results revealed an overarching subsidence velocity of -2.6 mm/yr across the entire study area. Grid cells situated within 50 km of the Texas shorelines exhibited a slightly reduced subsidence rate of -2.1mm/yr. Subsidence velocity near the shoreline grids further reduced down to around -1.0 mm/yr with an increasing trend at inland areas. Furthermore, this study documented heightened coastal flooding risks in specific local areas near the Texas shorelines, where the RSLR rate could reach up to 24.0 mm/yr. This rate was approximately seven times greater than the global sea-level rise rate observed between 1993 and 2014. Future investigations should concentrate on more accurate land motion mapping by combining observations from multiple SAR missions with different looking angles. Geospatial artificial intelligence methods should be leveraged to further investigate potential causes of subsidence at select hotspots. In addition, employing SBAS InSAR technique is worth exploration to focus on shoreline subsidence mapping with greater spatial coverage.

CRediT authorship contribution statement

Xiaojun Qiao: Conceptualization, Methodology, Data curation, Validation, Formal analysis, Investigation, Writing – original draft, Writing – review & editing. **Tianxing Chu:** Formal analysis, Writing – original draft. **Philippe Tissot:** Resources, Writing – review & editing. **Seneca Holland:** Writing – review & editing.

Declaration of competing interest

The authors declare that they have no known competing financial interests or personal relationships that could have appeared to influence the work reported in this paper.

Data availability

Data will be made available on request.

Acknowledgments

This research was supported by the U.S. Department of Commerce-National Oceanic and Atmospheric Administration (NOAA), USA through the University of Southern Mississippi (USM) under the terms of Agreement [No. NA13NOS4000166]. This work was also supported by the National Science Foundation (NSF), USA under award No. 2131263. The authors also thank the Open Access Publication Fund provided by the Mary and Jeff Bell Library at Texas A&M University-Corpus Christi (TAMU-CC). Opinions expressed by authors herein do not necessarily reflect views of NOAA, NSF or USM. The authors thank Jian Qing for successfully obtaining the lease production data of oil/gas wells from the Railroad Commission (RRC) of Texas.

Appendix A. Supplementary data

Supplementary material related to this article can be found online at https://doi.org/10.1016/j.jag.2023.103544.

References

- ASF, 2022. ASF data search vertex. URL https://asf.alaska.edu/, Copernicus Sentinel data. Retrieved from ASF DAAC [07/01/2022 of data access], processed by ESA.
- Bagheri-Gavkosh, M., Hosseini, S.M., Ataie-Ashtiani, B., Sohani, Y., Ebrahimian, H., Morovat, F., Ashrafi, S., 2021. Land subsidence: A global challenge. Sci. Total Environ. 778, 146193.
- Baker, E.T., 1979. Stratigraphic and Hydrogeologic Framework of Part of the Coastal Plain of Texas, Vol. 77. Texas department of water resources.
- Bertiger, W., Bar-Sever, Y., Dorsey, A., Haines, B., Harvey, N., Hemberger, D., Heflin, M., Lu, W., Miller, M., Moore, A.W., et al., 2020. Gipsyx/RTGx, a new tool set for space geodetic operations and research. Adv. Space Res. 66 (3), 469–489.
- Blewitt, G., Hammond, W., et al., 2018. Harnessing the GPS data explosion for interdisciplinary science. Eos 99.
- Bos, M., Fernandes, R., Williams, S., Bastos, L., 2013. Fast error analysis of continuous GNSS observations with missing data. J. Geod. 87 (4), 351–360.
- Buckley, S.M., Rosen, P.A., Hensley, S., Tapley, B.D., 2003. Land subsidence in Houston, Texas, measured by radar interferometry and constrained by extensometers. J. Geophys. Res.: Solid Earth 108 (B11).
- Castellazzi, P., Arroyo-Domínguez, N., Martel, R., Calderhead, A.I., Normand, J.C., Gárfias, J., Rivera, A., 2016. Land subsidence in major cities of Central Mexico: Interpreting inSAR-derived land subsidence mapping with hydrogeological data. Int. J. Appl. Earth Obs. Geoinf. 47, 102–111.
- Chen, X., Zhang, X., Church, J.A., Watson, C.S., King, M.A., Monselesan, D., Legresy, B., Harig, C., 2017. The increasing rate of global mean sea-level rise during 1993–2014. Nature Clim. Change 7 (7), 492–495.
- Chowdhury, A.H., Turco, M.J., 2006. Geology of the Gulf Coast Aquifer, Texas. In: Mace, R.E., Davidson, S.C., Angle, E.S., Mullican, W.F. (Eds.), Aquifers of the Gulf Coast of Texas: Texas Water Development Board Report. Texas Water Development Board, pp. 23–50.
- Church, J.A., White, N.J., 2006. A 20th century acceleration in global sea-level rise. Geophys. Res. Lett. 33 (1).
- Church, J.A., White, N.J., 2011. Sea-level rise from the late 19th to the early 21st century. Surv. Geophys. 32, 585-602.
- Cigna, F., Esquivel Ramírez, R., Tapete, D., 2021. Accuracy of sentinel-1 PSI and SBAS inSAR displacement velocities against GNSS and geodetic leveling monitoring data. Remote Sens. 13 (23), 4800.
- Colesanti, C., Ferretti, A., Prati, C., Rocca, F., 2003. Monitoring landslides and tectonic motions with the permanent scatterers technique. Eng. Geol. 68 (1–2), 3–14.
- Copernicus Climate Change Service, Climate Data Store, 2018. Sea level gridded data from satellite observations for the global ocean from 1993 to present. http://dx.doi.org/10.24381/cds.4c328c78, (Accessed 13 September 2023).
- Dinar, A., Esteban, E., Calvo, E., Herrera, G., Teatini, P., Tomás, R., Li, Y., Ezquerro, P., Albiac, J., 2021. We lose ground: Global assessment of land subsidence impact extent. Sci. Total Environ. 786, 147415.
- Douglas, B., Kearney, M.S., Leatherman, S.P., 2000. Sea Level Rise: History and Consequences. Elsevier.
- Du, Y., Feng, G., Li, Z., Peng, X., Zhu, J., Ren, Z., 2017. Effects of external digital elevation model inaccuracy on StaMPS-PS processing: A case study in shenzhen, China. Remote Sens. 9 (11), 1115.
- Elvidge, C.D., Zhizhin, M., Ghosh, T., Hsu, F.C., Taneja, J., 2021. Annual time series of global VIIRS nighttime lights derived from monthly averages: 2012 to 2019. Remote Sens. 13 (5), 922.
- Ferretti, A., 2014. Satellite inSAR Data: Reservoir Monitoring from Space (EET 9). European Association of Geoscientists & Engineers, URL https://www.earthdoc.org/content/books/9789462820036.
- Ferretti, A., Monti-Guarnieri, A., Prati, C., Rocca, F., Massonet, D., 2007. InSAR Principles-Guidelines for SAR Interferometry Processing and Interpretation, Vol. 19.
- Ferretti, A., Prati, C., Rocca, F., 2000. Nonlinear subsidence rate estimation using permanent scatterers in differential SAR interferometry. IEEE Trans. Geosci. Remote Sens. 38 (5), 2202–2212.
- Ferretti, A., Prati, C., Rocca, F., 2001. Permanent scatterers in SAR interferometry. IEEE Trans. Geosci. Remote Sens. 39 (1), 8–20.
- Galloway, D.L., Burbey, T.J., 2011. Review: Regional land subsidence accompanying groundwater extraction. Hydrogeol. J. 19, 1459–1486.
- Galloway, W.E., Hobday, D.K., Magara, K., 1982. Frio formation of Texas Gulf Coastal Plain: Depositional systems, structural framework, and hydrocarbon distribution. AAPG Bull. 66 (6), 649–688.
- Galloway, D.L., Jones, D.R., Ingebritsen, S.E., 1999. Land Subsidence in the United States, Vol. 1182. US Geological Survey.
- Gregory, J.L., 1966. A lower oligocene delta in the subsurface of southeastern Texas. Gulf Coast Assoc. Geol. Soc. Trans. 16, 227–241.

- Haley, M., Ahmed, M., Gebremichael, E., Murgulet, D., Starek, M., 2022. Land subsidence in the Texas coastal bend: Locations, rates, triggers, and consequences. Remote Sens. 14 (1), 192.
- Hu, J., Li, Z., Ding, X., Zhu, J., Zhang, L., Sun, Q., 2014. Resolving three-dimensional surface displacements from inSAR measurements: A review. Earth Sci. Rev. 133, 1–17
- Huang, S.A., Biondi, E., 2023. Towards improved time-series inSAR analysis with a multi-depth multi-focusing time-domain backprojection SAR algorithm. In: International Geoscience and Remote Sensing Symposium 2023.
- Hyne, N.J., 1984. Geology for Petroleum Exploration, Drilling and Production. Pennwell Books, Tulsa, OK.
- Kampes, B.M., 2014. Radar Interferometry: The Permanent Scatterer Technique, Vol. 12. Springer Dordrecht.
- Khan, S.D., Gadea, O.C.A., Tello Alvarado, A., Tirmizi, O.A., 2022. Surface deformation analysis of the houston area using time series interferometry and emerging hot spot analysis. Remote Sen. 14 (15), http://dx.doi.org/10.3390/rs14153831, URL https://www.mdpi.com/2072-4292/14/15/3831.
- Liu, Y., Wang, G., Yu, X., Wang, K., 2022. Sentinel-1 inSAR and GPS-integrated long-term and seasonal subsidence monitoring in Houston, Texas, USA. Remote Sens. 14 (23), 6184.
- Loucks, R.G., 1986. Controls on porosity and permeability of hydrocarbon reservoirs in lower tertiary sandstones along the Texas Gulf Coast. Virtual Landsc. Tex..
- Perissin, D., Wang, Z., Wang, T., 2011. The SARPROZ inSAR tool for urban subsidence/manmade structure stability monitoring in China. In: Proceeding of 34th International Symposium on Remote Sensing of Environment. ISRSE.
- Pratt, W.E., Johnson, D.W., 1926. Local subsidence of the Goose Creek oil field. J. Geol. 34 (7, Part 1), 577–590.
- Qiao, X., Chu, T., Tissot, P., Ali, I., Ahmed, M., 2023. Vertical land motion monitored with satellite radar altimetry and tide gauge along the Texas coastline, USA, between 1993 and 2020. Int. J. Appl. Earth Obs. Geoinf. 117, 103222.
- Qiao, X., Chu, T., Tissot, P., Louis, J., 2021. Land subsidence with tide gauge, radar altimetry and GNSS: A case study at subsiding coast in Texas. In: Proceedings of the 34th International Technical Meeting of the Satellite Division of the Institute of Navigation. ION GNSS+ 2021, pp. 3956–3962.
- Qiao, X., Chu, T., Tissot, P., Louis, J., Ali, I., 2022. Land subsidence estimation with tide gauge and satellite radar altimetry measurements along the texas Gulf Coast, USA. IEEE Geosci. Remote Sens. Lett. 19, 1–5.
- Qu, F., Lu, Z., 2022. Mapping deformation over greater houston using InSAR. Harris-Galveston Subsidence District. https://hgsubsidence.org/wp-content/uploads/2022/11/InSAR-Final-Report-2019-2021.pdf. (Accessed 8 July 2023).
- Qu, F., Lu, Z., Kim, J., Turco, M.J., 2023. Mapping and characterizing land deformation during 2007–2011 over the Gulf Coast by L-band InSAR. Remote Sens. Environ. 284, 113342.
- Qu, F., Lu, Z., Zhang, Q., Bawden, G.W., Kim, J.-W., Zhao, C., Qu, W., 2015. Mapping ground deformation over Houston–Galveston, Texas using multi-temporal InSAR. Remote Sens. Environ. 169, 290–306.

- Rajput, S., Thakur, N.K., 2016. Chapter 4 Tectonics and gas hydrates. In: Rajput, S., Thakur, N.K. (Eds.), Geological Controls for Gas Hydrate Formations and Unconventionals. Elsevier, pp. 107–130. http://dx.doi.org/10.1016/B978-0-12-802020-3.00004-7, URL https://www.sciencedirect.com/science/article/pii/B97801280202030000047
- Ramage, J.K., Braun, C.L., 2022. Status of Water-Level Altitudes and Long-Term and Short-Term Water-Level Changes in the Chicot and Evangeline (Undifferentiated) and Jasper Aquifers, Greater Houston Area, Texas, 2021. Technical Report, US Geological Survey.
- Ratzlaff, K., 1982. Land-surface subsidence in the Texas coastal region: Report 272. Harris-Galveston Subsidence District. http://www.twdb.texas.gov/publications/reports/numbered_reports/doc/r272/r272.pdf.
- RRC, 2023. The railroad commission of texas. https://www.rrc.texas.gov/. (Accessed 1 January 2023).
- SARPROZ, 2023. The SAR processing tool by periz. https://www.sarproz.com. (Accessed 1 January 2023).
- Shirzaei, M., Freymueller, J., Törnqvist, T.E., Galloway, D.L., Dura, T., Minderhoud, P.S., 2021. Measuring, modelling and projecting coastal land subsidence. Nat. Rev. Earth Environ. 2 (1), 40–58.
- Solís I, R.F., 1981. Upper tertiary and quaternary depositional systems, central coastal plain, Texas: Regional geology of the coastal aquifer and potential liquid-waste repositories. Virtual Landsc. Tex..
- Tay, C., Lindsey, E.O., Chin, S.T., McCaughey, J.W., Bekaert, D., Nguyen, M., Hua, H., Manipon, G., Karim, M., Horton, B.P., et al., 2022. Sea-level rise from land subsidence in major coastal cities. Nat. Sustain. 1–9.
- Teluguntla, P., Thenkabail, P., Oliphant, A., Gumma, M., Aneece, I., Foley, D., Mc-Cormick, R., 2023. Landsat-Derived Global Rainfed and Irrigated-Cropland Product 30 m V001. NASA EOSDIS Land Processes DAAC, http://dx.doi.org/10.5067/Community/LGRIP/LGRIP30.001. (Accessed 23 June 2023).
- TWDB, 2023. The Texas water development board (TWDB) groundwater database (GWDB). Online https://www3.twdb.texas.gov/apps/reports/GWDB/WaterLevelsAdvanced. (Accessed 1 July 2023).
- USGS, 2023. National water information system of United States geological survey (USGS). Online https://nwis.waterdata.usgs.gov/nwis/gwlevels. (Accessed 1 July 2023).
- Xu, X., Sandwell, D.T., Klein, E., Bock, Y., 2021. Integrated sentinel-1 InSAR and GNSS time-series along the San Andreas Fault system. J. Geophys. Res.: Solid Earth 126 (11), e2021JB022579.
- Younas, M., Khan, S.D., Qasim, M., Hamed, Y., 2022. Assessing impacts of land subsidence in Victoria County, Texas, using geospatial analysis. Land 11 (12), 2211.
- Yunjun, Z., Fattahi, H., Amelung, F., 2019. Small baseline InSAR time series analysis: Unwrapping error correction and noise reduction. Comput. Geosci. 133, 104331.
- Zhou, X., Wang, G., Wang, K., Liu, H., Lyu, H., Turco, M.J., 2021. Rates of natural subsidence along the Texas coast derived from GPS and tide gauge measurements (1904–2020). J. Surv. Eng. 147 (4), 04021020.